JOURNAL OF PROPULSION AND POWER
Vol. 23, No. 3, May–June 2007

# OH Planar Laser-Induced Fluorescence and Emission Imaging in High-Pressure LOx/Methane Flames

Ghislain Singla,* Philippe Scouflaire,† Juan Carlos Rolon,‡ and Sébastien Candel§
*Ecole Centrale Paris, CNRS, 92295 Châtenay-Malabry, France*
and
Lucien Vingert¶
*ONERA, 92322 Châtillon Cedex, France*

DOI: 10.2514/1.24895

**The application of planar laser-induced fluorescence of OH to high-pressure liquid oxygen/gaseous methane flames is investigated in this article. As pressure is increased, the maximum level of OH fluorescence decreases while an interfering light intensity increases. It is shown that suitable data can only be obtained by properly tuning the detection scheme. Narrowband filtering of OH fluorescence is required to reduce the level of interfering signals. An analysis of the interfering light indicates that it is associated with polycyclic aromatic hydrocarbon fluorescence originating from a region surrounding the flame. OH and polycyclic aromatic hydrocarbon fluorescence signal amplitudes become comparable at a pressure of 2.5 MPa which constitutes an upper bound for standard imaging. Below that limit the flame is well characterized and features thin, wrinkled OH layers developing in the vicinity of the liquid oxygen jet. The initial flame sheet is continuous but it becomes highly corrugated further downstream when the liquid oxygen jet breaks down. The flame edge standoff distance is greater than a few LOx post lip sizes indicating that stabilization is less well achieved than in the case of liquid oxygen/hydrogen flames where combustion typically begins at less than one lip size from the injector.**

## I. Introduction

HYDROXYL radicals fluorescence has been used in many recent combustion studies because OH is a key intermediate in hydrogen or hydrocarbon combustion chemistry and therefore constitutes an excellent flame marker. In nonpremixed flames, OH radicals are concentrated in thin layers indicating the position of the stoichiometric fuel/oxidizer surface where reaction takes place [1,2]. In premixed combustion, the OH mole fraction reaches its highest values in the flame front. Some OH also lingers in the hot combustion products formed by the flame, but the corresponding mole fractions are generally lower than those found in the reactive layer. These properties have been widely exploited to examine instantaneous flame structures. Spatial distributions of OH radicals are generally determined by planar laser-induced fluorescence (PLIF) imaging. This method has effectively provided two-dimensional visualizations allowing detailed investigations of laminar or turbulent flames and of many dynamical interactions between flow perturbations and reaction fronts [3]. Most of the previous OH fluorescence experiments were carried out at low or atmospheric pressure conditions and have concerned low heat release flames in laboratory scale devices, but applications have also been made at higher pressure mostly in internal combustion engines. There are few successful experiments on turbulent, high-power continuous combustors operating at elevated pressures. It is, however, of practical importance to consider intense flames in high-pressure environments. Detailed information is specifically needed if one wishes to address questions of importance to industrial gas turbines, aircraft engines, or rocket propulsion systems. It is not easy to apply OH–PLIF to high-pressure flames as indicated in various recent studies [4,5]. Many issues need to be considered, one of which is the choice of the excitation/detection scheme. One has to carefully select the excitation wavelength and take into account the frequency shift associated with pressure to optimize the absorption of light by the OH molecule [6]. It is also important to estimate effects of optical depth and quenching on the fluorescence signal to interpret the detected signals. Good quality images have been recorded with an acceptable signal to noise ratio [6] in the case of liquid oxygen/gaseous hydrogen flames ($LOx/GH_2$) at pressures ranging from 3.6 to 6.3 MPa. This required, in particular, an optimization of absorption of the laser fluence [6].

This article focuses on applications of planar laser-induced fluorescence imaging to high-pressure cryogenic combustion. The oxygen/methane propellant couple is specifically considered because it is envisaged for reusable liquid rocket engines. Design of these new systems requires an understanding of their combustion characteristics. The objective of the present investigation is to see if OH planar laser-induced fluorescence (OH–PLIF) can be used to examine the flame structure under high-pressure conditions and obtain images of the initial flame sheet. Emission of $CH^*$ radicals is also detected to obtain additional information on the flame shape and on its spreading rate. Experiments are carried out on the Mascotte cryogenic test bench at ONERA using a single shear coaxial injector. Liquid oxygen at a temperature and a pressure below critical is introduced in the chamber through the central tube. Gaseous methane is injected at high speed around the liquid oxygen stream. The flame structure is examined by combining images from OH–PLIF and $CH^*$ emission.

It will be shown in what follows that the performance of PLIF imaging obtained with $LOx/GH_2$ flames [6] cannot be matched with LOx/methane flames but for reasons which again differ from those expected at the beginning of this investigation.

It is commonly stated that quenching (collisional deexcitation) is the main factor which limits the application of laser-induced fluorescence under high-pressure conditions. It is shown in this article that interference from other fluorescence signals constitutes

Received 30 April 2006; revision received 8 July 2006; accepted for publication 9 July 2006. 

*Ph.D. Student, EM2C Laboratory, Ecole Centrale Paris; Current Address: Alstom, CH5401 Baden.
†Research Engineer, EM2C Laboratory, Ecole Centrale Paris.
‡Professor, ECP, EM2C Laboratory, Ecole Centrale Paris.
§Professor, ECP and Institut Universitaire de France, EM2C Laboratory, Ecole Centrale Paris; candel@em2c.ecp.fr. Fellow AIAA.
¶Research Engineer, DEFA BP 72.

the limiting factor. Good quality OH–PLIF images of highly turbulent cryogenic $LOx/GCH_4$ flames can be obtained up to pressures of about 2.5 MPa, but one has to filter out a nonresonant fluorescence interference. The source of this signal is investigated by examining its spectral content and characteristic features. It is shown that this interference originates from fluorescence from fuel fragments and polycyclic aromatic hydrocarbons (PAH) convected in the fuel rich regions surrounding the flame. The cryogenic $LOx/GH_2$ flame, free from such molecules, serves as a reference to show that interference is absent in that case. The present experiments indicate that the interference level increases with pressure and exceeds the OH fluorescence amplitude at about 3 MPa.

A description of the experimental setup and optical diagnostics is given in Sec. II. More details on LIF at high pressure are already discussed in [6] and will not be repeated here. The third section contains data recorded by exploring a range of pressures. The signal interfering with OH fluorescence is examined by making use of two alternate detection schemes. It is shown that a narrowband arrangement improves the signal to noise ratio. Issues for application to high-pressure, nonpremixed cryogenic flames are identified. A method is proposed which could be used to eliminate the interfering radiation and provide images of OH fluorescence with a reduced level of noise at pressures exceeding 2.5 MPa.

## II. Experimental Setup

The experimental combustion facility is only briefly described because many details are already given in previous articles [6,7].

High-pressure experiments are carried out on the cryogenic model scale combustion facility Mascotte. The chamber is equipped with a single coaxial injector used in previous studies. The inner duct conveys a low-speed liquid oxygen stream while methane or hydrogen flows in the outer annular duct. There is no recess and the two streams are confluent in the exhaust plane. The injector geometry appears on the left side of the PLIF and emission images discussed in the next sections.

The setup shown in Fig. 1 comprises an OH–PLIF system, an optical multichannel analyzer (OMA) for spectroscopic investigations, and light emission imaging using an intensified charge-coupled device camera (ICCD3) and another intensified CCD camera (ICCD2) to record light emission from $CH^*$ radicals.

The laser sheet used to pump the OH radical is generated by a Nd:YAG—pumped frequency doubled dye laser (Continuum Powerlite Precision II, Continuum ND6000, Continuum UVT-2) tuned to the $Q_{11}(9.5)$ transition of the $A^2\Sigma^+ - X^2\Pi$ ($v' = 1$, $v'' = 0$) band. The typical pulse energy in the UV around 284 nm is 42 mJ with a duration of 10 ns. The typical laser bandwidth full width at half-maximum (FWHM) is 0.15 $cm^{-1}$. The UV laser beam is expanded to a diameter of 5 mm. As shown in Fig. 1, a spherical convergent lens ($f_{S1} = 860$ mm, UV 284 nm) associated with a UV grade fused silica cylindrical divergent lens ($f_{C1} = -75.6$ mm) and two mirrors M1 ($\phi = 25$ mm, UV 284 nm), M2 ($120 \times 25$ $mm^2$, UV 284 nm) are used to form the incident laser beam into a thin sheet. The telescope setup is employed to expand the beam in one dimension forming a narrow sheet of light which is then focused in the chamber. Sheet dimensions are approximately $8d_{LOx}$ by 500 $\mu$m. The wings of the laser beamshape are not used to illuminate the region of interest so that the intensity in the sheet is nearly constant. For the laser output and for this light sheet geometry, the power density is of the order of 15 MW $cm^{-2}$.

The fluorescence signal is collected by a Princeton Instruments 5 MHz ICCD camera with a 120 $\mu$m resolution (closeup on the injector near field) at a rate of 10 Hz. The exposure time is fixed at a value of 50 ns. The intensifier is used to gate the fluorescence signal to achieve a higher signal to noise ratio. Light is collected by a UV Nikkor 105 mm/$f$4.5 objective. The ICCD camera placed at right angles to the flow direction in the chamber is equipped with filter sets FS1 or FS2 defined later in this section (see Table 1).

### A. Filtering Schemes for OH Fluorescence Detection

Two schemes are used to filter the light radiated by the flame (Table 1). The first scheme FS1 combines a WG305 to block light scattered by the liquid jet in combination with a UG11 bandpass filter. The UG11 colored glass filter passes a peak wavelength of 340 nm and has a bandpass wavelength range extending from 245 to 390 nm. The pair transmits about 56% of the incident radiation in the band between 306 and 320 nm. The bandpass filter also passes light above 650 nm and has a residual peak transmittance at 720 nm of 5%. This broadband filter set was initially selected because of its greater light collection efficiency over narrowband filtering. Similar broadband schemes have been effectively used in previous hydrocarbon flame studies [2] and in $LOx/GH_2$ cryogenic combustion experiments [8], apparently without interference problems from undesired signals.

The second scheme FS2 associates two WG305 and a narrowband interference filter with a peak transmittance of 25% at 308 nm and a FWHM of 15 nm. The total transmittance is about 22%.

### B. Emission Spectroscopy and Imaging

Spectroscopic measurements are delayed by 1 $\mu$s to eliminate any fluorescence signals. Light is detected by an optical multichannel

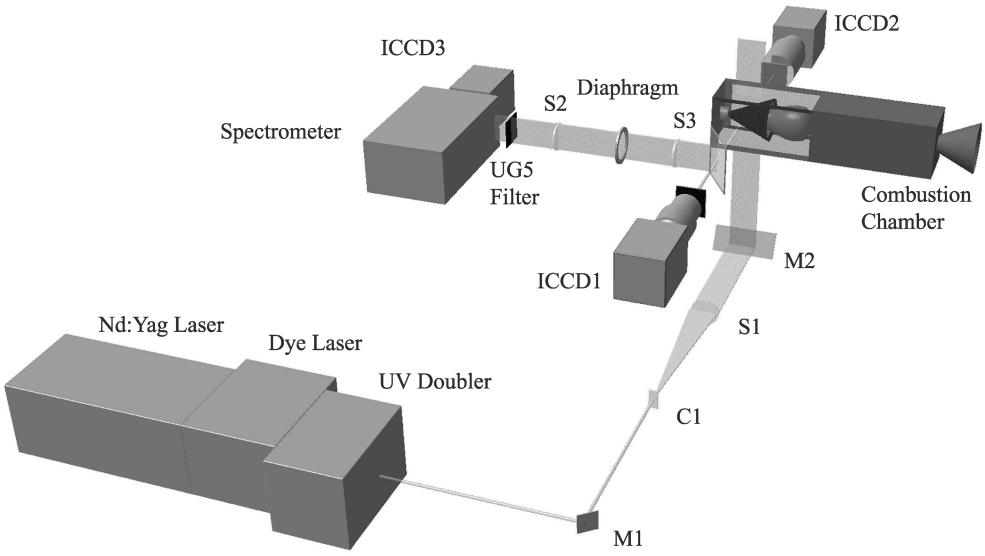


**Fig. 1 Schematic representation of the experimental setup for simultaneous OH PLIF, spectral analysis, and $CH^*$ light emission imaging. The fluorescence signal is detected by camera ICCD1 equipped with filter sets FS1 or FS2. Emission from $CH^*$ radicals is detected by ICCD2 equipped with filter set FSE. Spectral data are obtained from the optical multichannel analyzer equipped with camera ICCD3.**

**Table 1 Characteristics of the filtering schemes tested in this study**

| Filtering scheme | Detection objective | Filter combination | Spectral ranges | Pressure limitation |
|---|---|---|---|---|
| FSE | CH* $A-X(0,0)$ | SWP604<br>FCG059 | 420–440 nm with a maximum $I/I_0$ of 0.9 | No pressure limitations as chemiluminescence increases with pressure. |
| FS1 | OH $A-X(1,1)$ | WG305 | 280–390 nm with a maximum $I/I_0$ of 0.8 at 315 nm | Up to 2.1 MPa |
| | OH $A-X(0,0)$ | UG11 | 660–800 nm with a maximum $I/I_0$ of 0.02 at 700 nm | Light scattered by the liquid jet is partially transmitted. |
| FS2 | OH $A-X(1,1)$ | WG305 ×2 | 300–315 nm with a maximum $I/I_0$ of 0.22 at 308 nm | Up to 3.2 MPa |
| | OH $A-X(0,0)$ | 308BP15 | | |

analyzer (OMA) (Acton Spectra Pro 2500i, 500 mm focal length) fitted with a Princeton Instruments ICCD camera $1024 \times 1024$ pixels. Spontaneous OH* emission is collected by two convergent spherical UV grade fused silica lenses ($f_{S2} = 650$ mm, $f_{S3} = 1200$ mm) and projected on the slit ($h_{\text{slit}} = 14$ mm, $\delta_{\text{slit}} = 20$ $\mu$m) of the OMA. The second order of the grating is eliminated using a UG5 filter (400 nm low pass filter) placed in front of the entrance slit thus effectively increasing the spectral resolution. Light transmitted through the slit is scattered by a 2400 grooves/mm grating providing a spectral resolution of about 0.01 nm per pixel. The spatial resolution is defined by the lens magnifying power and the ICCD sensor. Emission from the $A-X(0,0)$ is analyzed by positioning the grating at the median value of the vibrational band involved. Light emission is collected, projected on the CCD sensor, and spectrally dispersed. The flame slice described by OH* spontaneous emission is spatially and spectrally resolved with this system. Data gathered at high pressure may be compared with reference spectra obtained in an atmospheric pressure experiment on a $GO_2/GCH_4$ nonpremixed flame and with numerical spectral estimates synthesized with Lifbase [9]. Spontaneous emission of CH* is detected at a rate of 10 Hz with the ICCD2 camera with a useful resolution of $236 \times 422$ pixels. The camera is equipped with a visible Nikon 80–200 mm $f = 2.8$ objective providing a full view of the visualization window. A SWP604 glass filter blocks radiations above 450 nm and a FCG-059 glass filter suppresses radiations below 400 nm, while passing 90% of the light emitted between 420 and 440 nm where CH* chemiluminescence is observed. These characteristics are gathered in Table 1. This filtering scheme designated in what follows as the filtering scheme for emission (FSE) should not be confused with the filter combinations described below. The exposure time is fixed at 1 $\mu$s to capture nearly instantaneous images with a high $S/N$ value. In most experiments the two cameras ICCD1 and 2 are triggered synchronously but in some cases ICCD2 was delayed by 1 $\mu$s with respect to ICCD1 to eliminate fluorescence signals induced by the laser pulse.

## III. High-Pressure Imaging

Results of OH–PLIF imaging are now discussed. Measurements are carried out on $LOx/GCH_4$ cryogenic jet flames at pressures between 1 and 3 MPa. Beyond 2.5 MPa the signal to noise ratio becomes too low to retrieve any useful information. It is shown in what follows that as pressure increases, a nonresonant background interference progressively reduces the signal to noise ratio. Combinations of glass filters (discussed above) and bandpass filters are used to optimize the OH $A-X(0,0)$ and $A-X(1,1)$ fluorescence collection efficiency while minimizing interference levels. It will be shown that the parasitic signal is associated with the presence of hydrocarbon products of the oxygen/methane reaction.

### A. $LOx/GCH_4$ Flame at 1 MPa

It is interesting to first examine images obtained under low-pressure conditions. Typical time histories of injection parameters of a $LOx/GCH_4$ hot fire test are displayed in Fig. 2 and in Table 2. The desired value of the chamber pressure is fixed by a convergent divergent choked nozzle and by the liquid oxygen and gaseous methane mass flow rates. The chamber pressure is in this case well below the critical value of oxygen $p < p_c(O2) = 5.04$ MPa, and the injected oxygen stream undergoes a cascade of processes associated with breakup, atomization, vaporization, and combustion. Typical distributions of OH fluorescence intensity are recorded in this case with the first filtering scheme (FS1).

Images obtained with the filtering scheme FS1 (detection between 305 and 390 nm) are shown in Fig. 3. In these images and in all others discussed in this article the laser sheet extends over $8d_{\text{LOx}}$. The signal to noise ratio is high and the flame structure is well defined in the lower half and to a lesser extent in the upper half of the chamber. As the optical depth of the medium decreases with pressure, the laser beam is attenuated while crossing the first OH layer before being partially distorted by the high-density liquid oxygen explaining the reduced level of fluorescence intensity in the upper flame layer. The

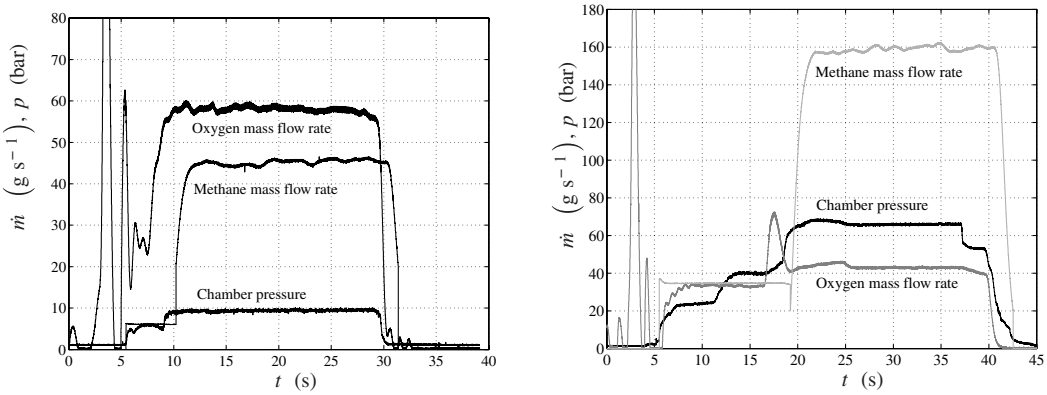


**Fig. 2 Left: injection parameters, during the low-pressure hot fire test (point G in Table 2). Right: injection parameters corresponding to points A–F. Three steady pressure levels are also obtained during this test, a low pressure $p = 2.5$ MPa, a medium pressure $p = 4$ MPa, and a high pressure $p = 6.5$ MPa. The second pressure stage is reached by injecting helium to cool the visualization windows.**

**Table 2 Hot fire operating conditions. Points A–F are obtained by progressively increasing the oxygen mass flow rate while keeping the methane flow rate at a constant value. Point G corresponds to a low-pressure steady-state operation ($p = 0.94$ MPa). Point H is obtained by injecting hydrogen in place of methane. The last column in this table gives the mixture ratio $E = \dot{m}_{\mathrm{LOx}}/\dot{m}_F$**

| No. | Fuel | $\dot{m}_{\mathrm{LOx}}$, gs$^{-1}$ | $\dot{m}_F$, gs$^{-1}$ | $p$, MPa | $E$ |
|---|---|---|---|---|---|
| A | $GCH_4$ | 8.2 | 34.5 | 1.5 | 0.23 |
| B | $GCH_4$ | 10.3 | 34.5 | 1.6 | 0.3 |
| C | $GCH_4$ | 13.1 | 34.5 | 1.7 | 0.38 |
| D | $GCH_4$ | 15.9 | 34.5 | 1.8 | 0.46 |
| E | $GCH_4$ | 21.5 | 34.5 | 2. | 0.62 |
| F | $GCH_4$ | 24.3 | 34.5 | 2.1 | 0.7 |
| G | $GCH_4$ | 58.1 | 45.2 | 0.94 | 1.3 |
| H | $GH_2$ | 92 | 50 | 6.3 | 1.86 |

distribution of light intensity is relatively thick and some signals originate from the inner side of the flame indicating that a residual part of the light scattered by the liquid jet is detected by the camera. The scattered signal is so intense that it is only partially rejected by the filtering scheme FS1. In the injector near field the flame is well anchored to the injector lip and spreads from this point into the chamber. The flame sheet initially follows the liquid jet boundary [8,10] and the geometry is quite similar to that found in $LOx/GH_2$ cryogenic flame experiments [8] carried out in the same range of pressures (up to 1 MPa). Further downstream the OH layer spreads outward and features wrinkles and isolated pockets.

It is interesting to compare the OH–PLIF images to instantaneous $CH^*$ emission data (Fig. 4) recorded with the wide field ICCD2 camera. The spontaneous emission of $CH^*$ $A^2\Delta - X^2\Pi$ (0,0) around 430 nm is collected simultaneously with OH fluorescence by triggering the two cameras with the same TTL signal.

An established flame appears in the emission images but there are some less standard features. In the first region the flame is close to the liquid jet and spreads progressively outward. The liquid jet atomization generates droplets which are dispersed by turbulence associated with the high-speed annular gaseous stream. The flame expands sharply at the point where the liquid jet breaks down. It was shown [11] that the gaseous stream momentum flux had to be sufficiently large with respect to the liquid oxygen momentum flux to correctly atomize the liquid jet. This in turn gives rise to a flame of the type observed in the present case. A careful analysis of the instantaneous $CH^*$ images in the fuel rich region reveals a broad outer region ($0 < x/d_{\mathrm{LOx}} < 4$, $0.5 < r/d_{\mathrm{LOx}} < 3$) of relatively low signal amplitudes of approximatively 10% of that of the maximum $CH^*$ intensity. The presence of light radiation in this external region is clearly revealed in the average light intensity field (Fig. 5) obtained by summing an ensemble of instantaneous emission images. The axial extent of this region nearly coincides with that of the laser sheet. The instantaneous and average images feature two different types of light distributions. The first corresponds to a standard flame stabilized on the injector lip while the second is formed by an interference signal originating from the outer region bordering the methane stream where fuel and combustion products mix and recirculate. The recirculation region cannot be deduced from the previous data but is made apparent by liquid water streaks on the lateral windows. This region extends from the backplane to about $10d_{\mathrm{LOx}}$. A radial slice of fluorescence and emission distributions recorded in the injector near field at a distance $x/d_{\mathrm{LOx}} = 2$ is displayed in Fig. 6. The maximum intensity associated with OH fluorescence and $CH^*$ light emission coincide at $r/d_{\mathrm{LOx}} = 0.32$. The $CH^*$ emission intensity distribution is nearly symmetrical with respect to the injector axis whereas the OH fluorescence intensity profile is skewed. The lack of symmetry in OH fluorescence is due to partial absorption of the laser light as it crosses the first flame situated on the laser sheet input side and to scattering of the incident beam by the liquid oxygen stream. The emission signal collected between 420 and 440 nm features two additional maxima located in the fuel rich regions close to the methane stream at a distance of $r/d_{\mathrm{LOx}} = 1.3$ from the axis. Other experiments in which the camera ICCD2 is delayed with respect to the laser pulse by 1 $\mu$s show no light radiation in the outer flame region. These data indicate that light is emitted from the region surrounding the methane stream and that it is induced by the laser pulse. We will see that this radiation is most probably due to fluorescence of species formed by methane decomposition in the intermediate temperature gaseous products recirculating near the injection plane.

At this point it is worth examining data recorded by the OMA in a spectral range extending from 306 to 314 nm. It is first useful to examine a spectrum recorded at low pressure (0.1 MPa) on a flame formed by coaxial injection of gaseous oxygen and methane (Fig. 7). One recognizes the standard (0-0) emission band of OH. When this is compared to a numerically synthesized spectrum calculated with Lifbase one finds an excellent match for line positions, widths, and spectral density.

At 0.9 MPa and under cryogenic injection conditions the optical multichannel analyzer provides data displayed in Fig. 8. The wavelength is used as a horizontal coordinate while the ordinate corresponds to the radial position measured with respect to the jet axis. The $x = 0$ position defines the injection plane. The OH $A^2\Sigma \rightarrow$

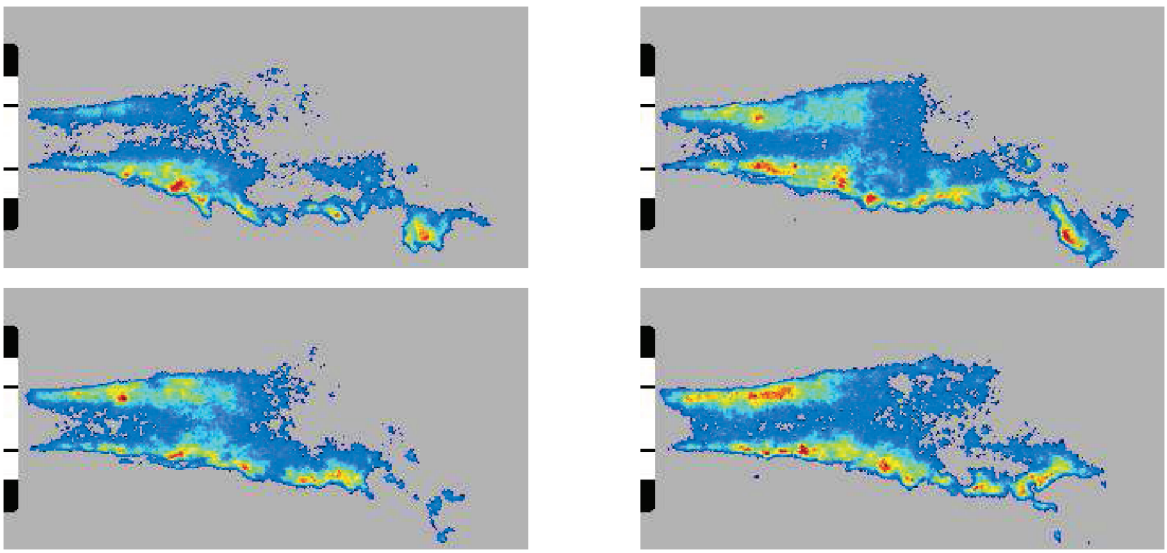

**Fig. 3 Fluorescence of OH recorded in the injector near field at 0.94 MPa, $\dot{m}_{\mathrm{LOx}} = 58$ gs$^{-1}$, $\dot{m}_{\mathrm{CH4}} = 45$ gs$^{-1}$ (point G). The exposure time is 50 ns. The flame is well anchored on the injector lip. The filtering scheme FS1 transmits a residual amount of laser light scattered by the liquid oxygen jet.**

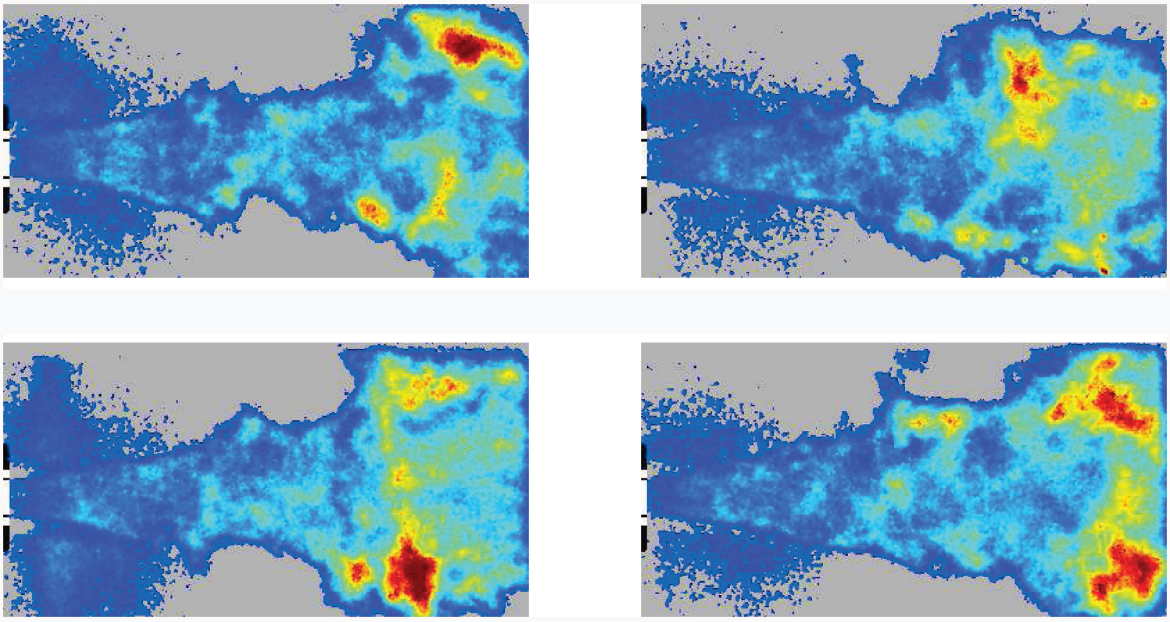

**Fig. 4 Typical emission images $t_{exp} = 1\ \mu s$, $p = 1$ MPa, $\dot{m}_{LOx} = 58\ gs^{-1}$, and $\dot{m}_{CH4} = 45\ gs^{-1}$ (point G). Emission images show that radiation originates from the near vicinity of the coaxial injector indicating that the flame is stabilized on the LOx injector lip and spreads in a standard fashion. A signal emitted from the flame surroundings is also detected in a region extending over an axial distance which is approximately equal to the size of the laser sheet. The shutter opening is synchronized with the laser pulse.**

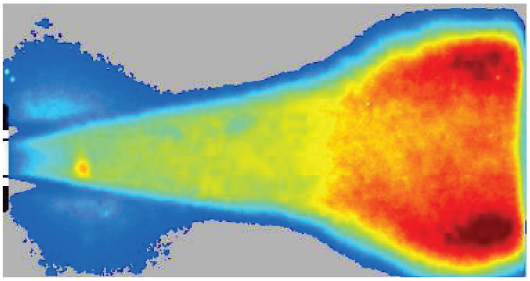

**Fig. 5 Average image obtained by summing emission instantaneous images $p = 0.94$ MPa, $\dot{m}_{LOx} = 58.1\ gs^{-1}$, and $\dot{m}_{CH4} = 45.2\ gs^{-1}$ (point G). A signal originating from a region surrounding the methane stream is detected. The axial extent of the radiating outer region is equal to the laser sheet used to excite the OH radical in the UV range.**

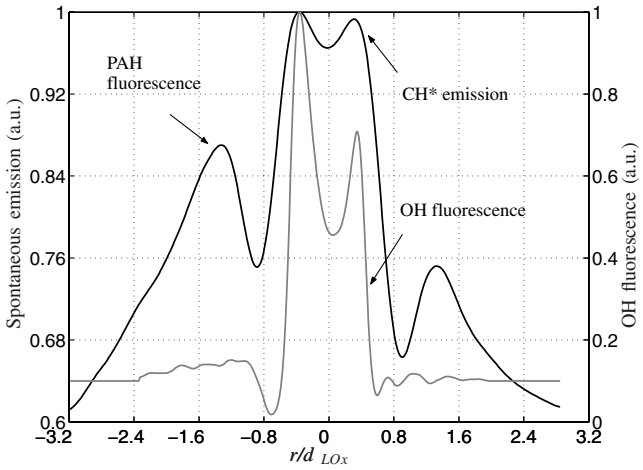


**Fig. 6 Fluorescence intensity profile and light emission distribution in a slice of the flame in the injector near field ($x/d_{LOx} = 2$). The emission profile is deduced from Fig. 5. The high-temperature oxidation region is located at $r/d_{LOx} = 0.6$ while the fluorescence of hydrocarbon fuel fragments in the visible range originates from the outer boundary of the methane stream at $r/d_{LOx} = 1.3$. Positive and negative values of the radial coordinate, respectively, correspond to the lower and upper parts of the chamber. $p = 0.94$ MPa, $\dot{m}_{LOx} = 58.1\ gs^{-1}$, $\dot{m}_{CH4} = 45.2\ gs^{-1}$ (point G).**

$X^2\Pi$ ($v' = 0$, $v'' = 0$) emission bands are well apparent and the corresponding patterns of spectral lines are detected at the radial position of the flame. This is also made evident in Fig. 9 where OH* emission lines are easily identified.

Analysis of the spectra reveals that there is a continuum of radiation in the same wavelength band as can be seen by comparing experimental and synthesized spectra (Fig. 9). The relative intensity of each line is displaced to a higher value by about 20%. This indicates the presence of broadband emission from soot. Each line of the (0,0) band of emission is also wider than expected from standard calculations indicating that collisional broadening close to the flame front is enhanced by the existence in that region of larger molecular weight fuel fragments like PAH which act as soot precursors.

### B. Higher Pressures (1 to 3 MPa) LOx/GCH$_4$ Experiments

The pressure is initially stabilized around $p = 2.1$ MPa. Typical OH fluorescence distributions collected with the filter set FS1 are shown in Fig. 10. An interfering signal generated outside the methane stream is now quite visible. The laser sheet is also attenuated as it propagates through the medium and fluorescence is mainly

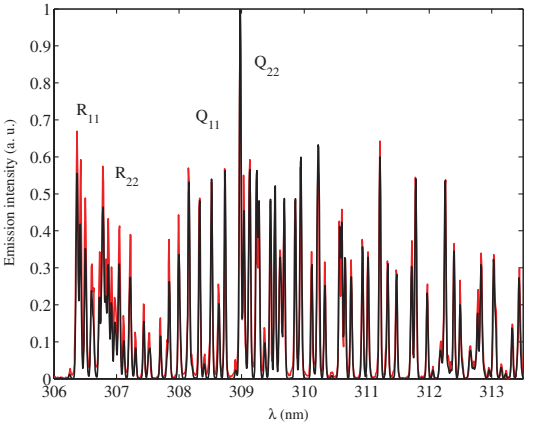


**Fig. 7 Black line: Emission spectra $A^2\Sigma - X^2\Pi$ (0,0) of OH plotted at the flame front. Red line: synthetic spectra computed with Lifbase at 3000 K and 0.1 MPa using a Voigt profile to take into account the collisional and Doppler broadening.**

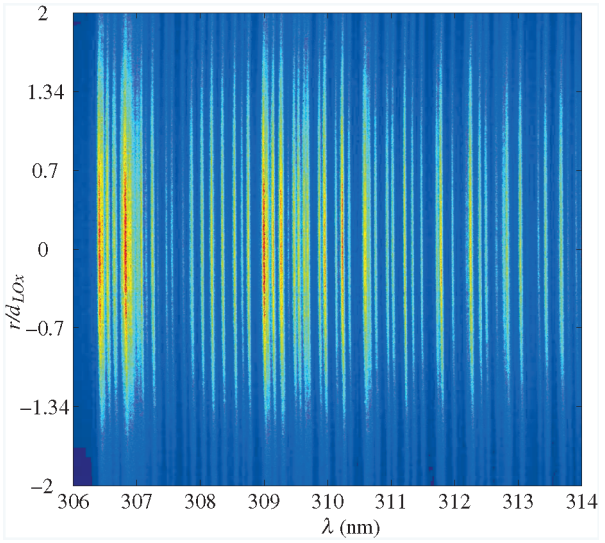


**Fig. 8 Spatial distribution and wavelength dispersion of radiation detected by the OMA. The OH characteristic $A^2\Sigma - X^2\Pi$ (0,0) band emission is displayed. The radial slice is located at $x/d_{\mathrm{LOx}} = 5$ from the injection plane.**

detected in the lower half of the domain. The parasitic fluorescence signal is so intense in this region that it uses most of the dynamic range of the imaging system. Instantaneous emission images acquired simultaneously are saturated in the region crossed by the laser sheet and not shown for this reason.

Figure 11 gives a radial distribution of the intensity signal collected between 305 and 390 nm. This profile features two peaks of light intensity, the first close to the oxygen liquid jet corresponding to OH fluorescence is reached at $r/d_{\mathrm{LOx}} = 0.32$; the second, more intense is located near the methane stream in the outer region at $r/d_{\mathrm{LOx}} = 1.3$. The spatial distributions of OH fluorescence and interference signals have similar shapes but are spatially distinct. On the lower side of the PLIF images which correspond to the laser transmission side OH fluorescence levels at pressures in excess of 1.5 MPa are lower than those of the parasitic fluorescence originating from the flame surroundings.

When the second set of filters FS2 is employed, one obtains the set of images shown in Fig. 12 which correspond to pressures between 1.5 and 2.1 MPa. The signal to noise ratio is enhanced and well defined PLIF images are recorded by the camera. The laser light scattered by the oxygen jet is eliminated indicating that the narrowband filtering scheme FS2 completely rejects this intense radiation. Fluorescence from OH thus becomes the major contributor to the light intensity in the flame region. The OH layer begins in the

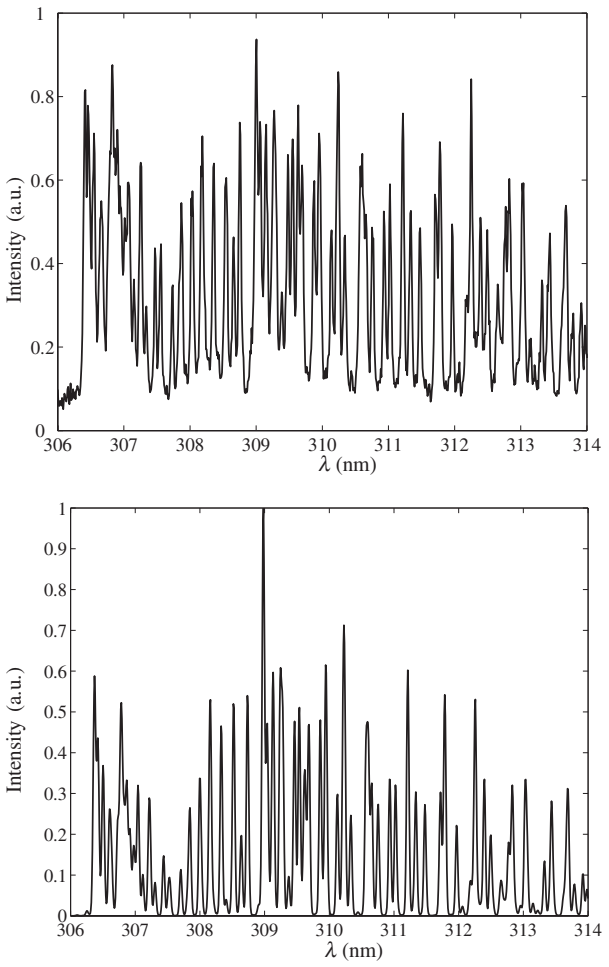


**Fig. 9 Top: (0,0) band of emission detected in the LOx/GCH4 experiment at 0.94 MPa; $r/d_{\mathrm{LOx}} = 0.6$. Bottom: OH emission spectrum synthesized by Lifbase using Voigt profiles at 2400 K and 0.94 MPa.**

vicinity of the injector lip but the flame edge position fluctuates and its average distance equals about 4 times the LOx post thickness. The OH layer features wrinkles and pockets further downstream and it becomes highly corrugated with thickened braids and some isolated pockets.

At higher pressures, the background intensity signal increases while the OH fluorescence level decreases. At $p = 3$ MPa, the image (see Fig. 13) exhibits severe, nonresonant UV laser absorption, which is reflected in the spatial light distribution. Intense radiation

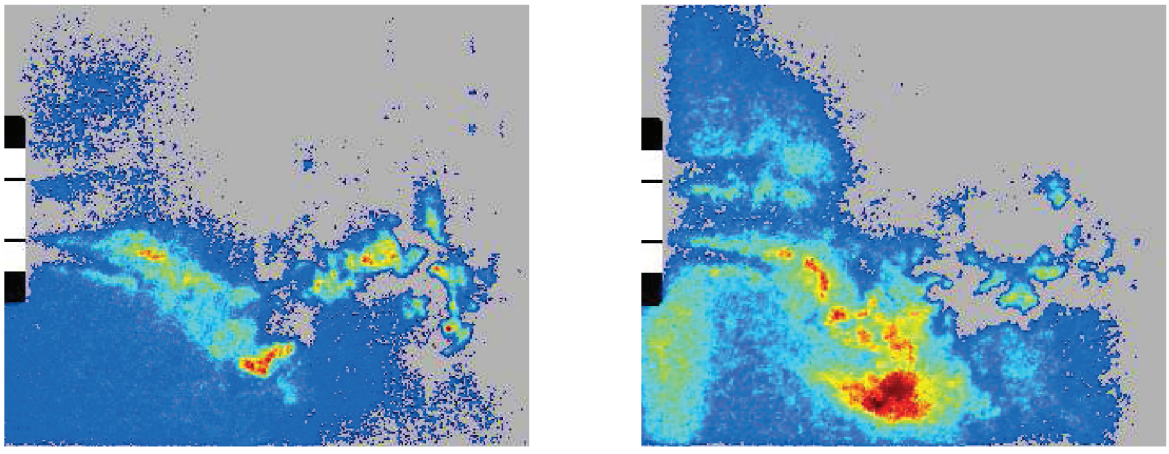

a) b)

**Fig. 10 OH PLIF images $\mathrm{LOx/GCH_4}$ cryogenic flame, $p = 2.1$ MPa. The fluorescence signal is collected with the filtering scheme FS1. The interference level exceeds that of the OH fluorescence signal.**

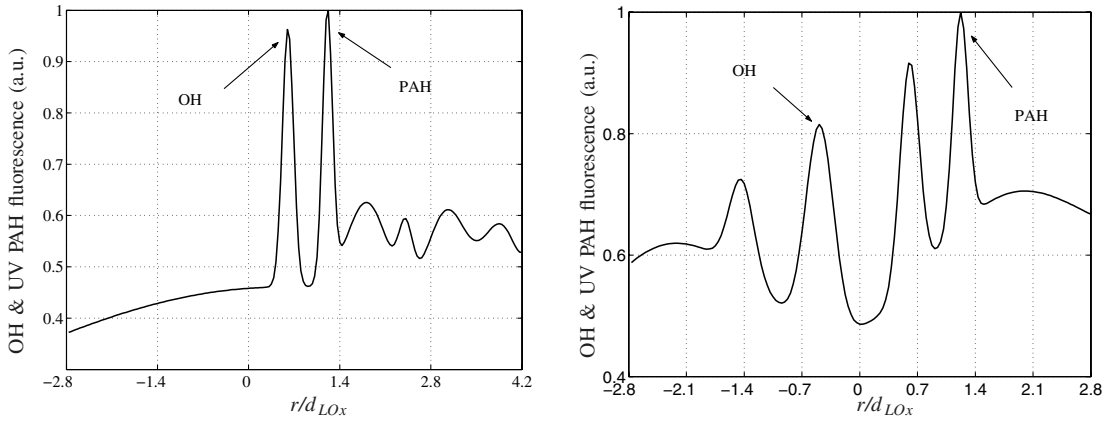


**Fig. 11 Profiles showing OH and UV PAH fluorescence distributions in one axial section $x/d_{\mathrm{LOx}} = 2$. The high-temperature oxidation region is located at $r/d_{\mathrm{LOx}} = 0.6$ while hydrocarbon pyrolysis takes place near the outer boundary of the methane gaseous stream at $r/d_{\mathrm{LOx}} = 1.3$. Positive and negative values of the radial coordinate, respectively, correspond to the lower and upper parts of the chamber. Left: the slice is deduced from Fig. 10a. Right: the slice is obtained from Fig. 10b.**

originates from the flame reactive layers and from its outer surroundings. Beyond 3 MPa, the interference signal overwhelms the OH fluorescence signal and one cannot hope to retrieve useful information from the luminous background.

### C. High-Pressure OH–PLIF in a Cryogenic $\mathrm{LOx/GH_2}$ Flame

To make certain that the interfering light signal is associated with the presence of hydrocarbons, the same PLIF experiments were repeated by replacing methane by gaseous hydrogen. The objective was to see whether the interference would still occur in a hydrocarbon free flame (Fig. 14). Typical distributions of OH fluorescence intensity collected with the second set of filters FS2 in high-pressure $\mathrm{LOx/GH_2}$ experiments are displayed in Fig. 15. At the operating pressure of 6.3 MPa the signal to noise ratio is quite acceptable but somewhat lower than that obtained at low pressure. There is no background noise of the type found in the $\mathrm{LOx/GCH_4}$

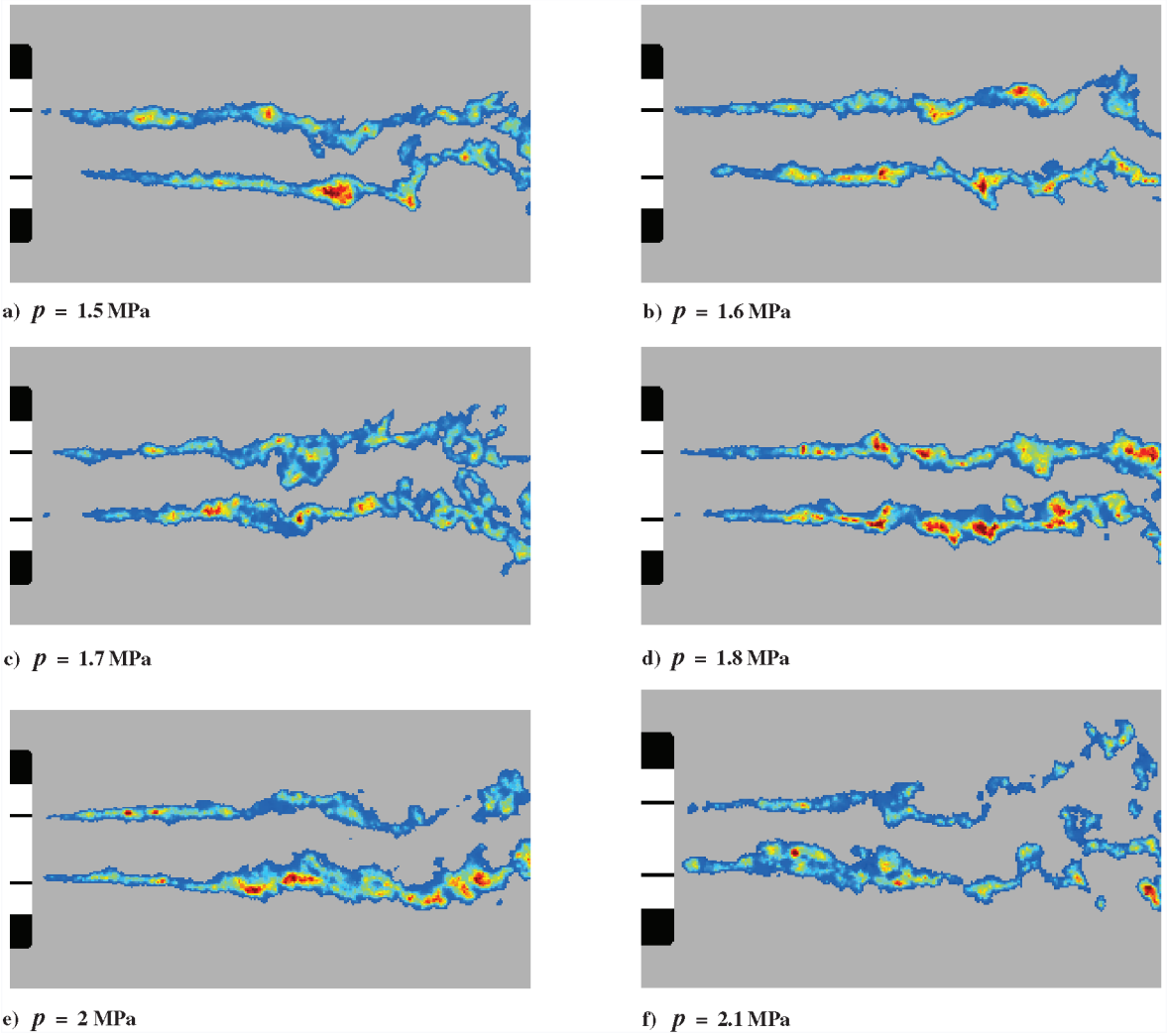


**Fig. 12 OH PLIF images in $\mathrm{LOx/GCH_4}$ cryogenic flames, $1.5 \leq p \leq 2.1$ MPa (points A–F). Fluorescence is collected with the set of filters FS2. The laser sheet extends over $8d_{\mathrm{LOx}}$ from the injector plane.**

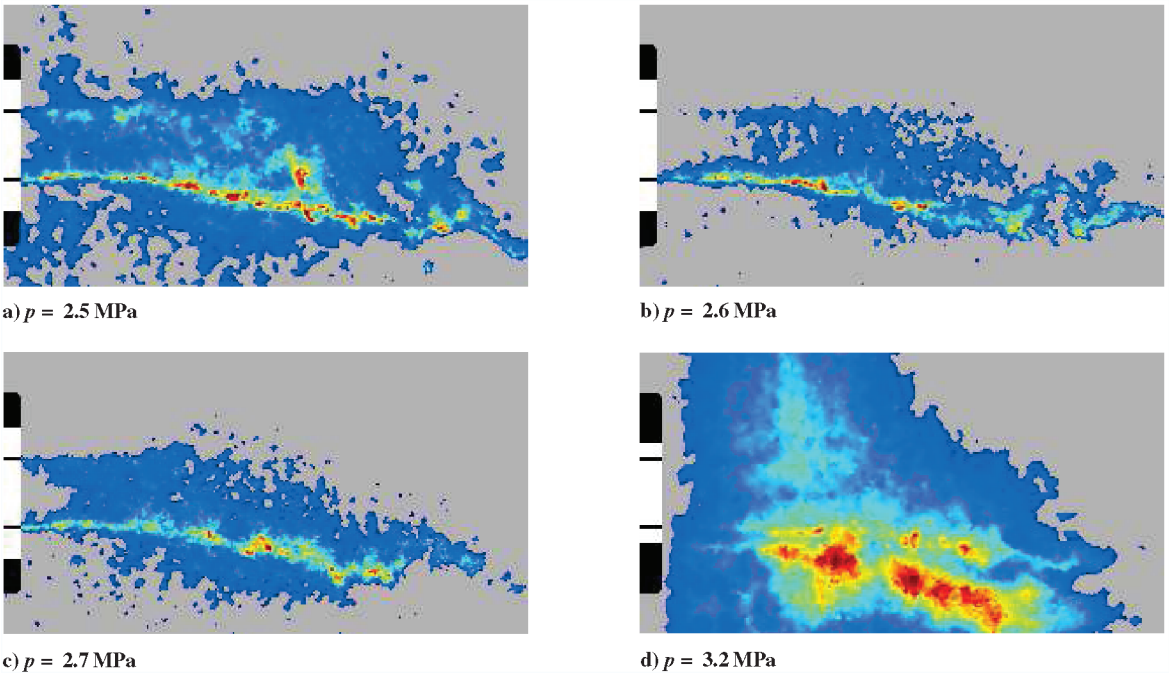


**Fig. 13 PLIF images of $LOx/GCH_4$ cryogenic flames, $2.5 \leq p \leq 3$ MPa. The fluorescence signal is collected with filter scheme FS2. At $p = 3.2$ MPa, the image exhibits a strong interference signal and severe nonresonant attenuation, which is reflected in the reduction of the signal on the upper side of the chamber.**

tests indicating without ambiguity that interference is due to the presence of hydrocarbon molecules generated by methane decomposition and combustion.

The flame structure in this high-pressure $LOx/GH_2$ experiment differs to some extent from that found in the lower pressure $LOx/GCH_4$ experiments because the oxygen stream now undergoes a transcritical change of state. The chamber pressure exceeds the critical value of oxygen [6,7]. In the injector near field, the flame features two regions. In the first the reaction layer spreads inward and it is fairly smooth. In the second region the flame expands outward in a more progressive manner and features wrinkles and pockets similar to those detected at lower pressures in the $LOx/GCH_4$ experiments.

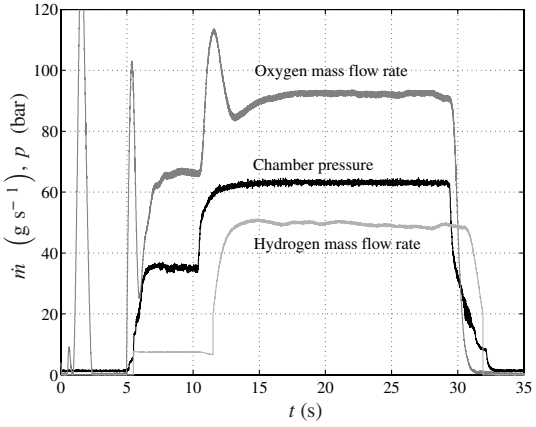


**Fig. 14 Injection parameters $LOx/GH_2$ cryogenic flame. Two pressure stages can be analyzed, an intermediate pressure at $p = 3.6$ MPa and a high pressure at $p = 6.3$ MPa (point H).**

## VI. Discussion

Experiments on $LOx/GCH_4$ flames reported in this article indicate that laser-induced fluorescence of OH is detectable but subject to an interference signal originating from the region surrounding the flame and bordering the methane jet.

The source of the interference and associated laser attenuation has been attributed to induced fluorescence from PAH molecules. One should, however, consider the possibility that the signal originates from another process such as laser-induced incandescence. Table 3 lists a few characteristics of these two types of interactions. One notable difference between PAH–LIF and soot-LII is that the latter requires a high laser fluence to obtain particle incandescence [12–14]. Here, both the low laser fluence and the spectral content of the signal are not consistent with laser-induced incandescence of soot particles. On the other hand, fluorescence from hydrocarbon fragments and PAH has the expected features. Fluorescence originating from PAH has been detected in a variety of spray and gaseous diffusion flames [14–18] and in chemical vapor deposition experiments [19]. The corresponding signal is known to interfere with optical measurements of other species. PAH molecules typically appear during the low temperature pyrolysis of hydrocarbon fuels and have a strong propensity to absorb UV radiation. Absorption and emission depend on the vibrational energy levels of these molecules. It is known that the emission spectra and the spectral location of the maximum PAH fluorescence depends on the excitation wavelength. In the present case pumping takes place in

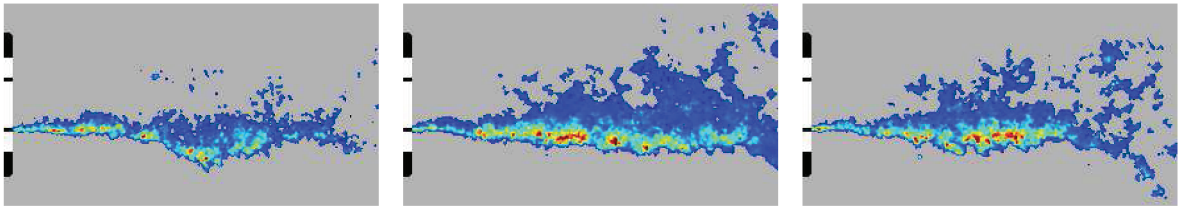

**Fig. 15 OH PLIF images in the injector near field recorded in $LOx/GH_2$ cryogenic combustion experiments at a pressure $p = 6.3$ MPa, $\dot{m}_{LOx} = 92$ gs$^{-1}$, and $\dot{m}_{H2} = 50$ gs$^{-1}$ (point H). There is no interference in these images but the optical depth is limited by absorption in the OH layer.**

**Table 3 Main characteristics of PAH fluorescence and laser-induced incandescence technic**

| Main characteristics | PAH LIF | LII |
|---|---|---|
| Spectral content | Components in the UV and visible range | Broadband radiation |
| Pressure dependence | Increases with PAH mole fraction which increases with pressure | Increases with soot volume fraction which increases with pressure |
| Laser fluence | Signal is proportional to laser fluence | Requires high levels of laser fluence to induce incadescence |
| Signal detection | Approximately equal to laser pulse duration | Approximately equal to 700 ns |

the UV range. It is known from previous studies [18,20] in which low power excitation was used in the range 280–290 nm or at 266 nm that fluorescence from regions of pyrolysis features a broadband spectrum, extending from the UV to the visible range (from 300 to 500 nm). This type of radiation is exemplified in a study of n-heptane diffusion flames at 0.1 MPa [16]. For these conditions, the fluorescence spectra have been related to PAH species which extend their emission bands toward visible wavelengths according to the number of aromatic rings. This is also observed in some strained diffusion flame experiments where the OH fluorescence peak is found on the oxidizer side while PAH fluorescence is detected on the fuel side of the flame [18]. This is confirmed by experiments in which naphtalene placed in a cell at high temperature and excited in the UV features a fluorescence spectrum characterized by two peaks, one in the UV near 330 nm and the second, in the visible range, near 430 nm.

Fluorescence experiments on cryogenic $LOx/GCH_4$ combustion at high pressure exhibit a broadband emission spectrum. The UV excitation near 284 nm induces light emission with a first contribution in the UV range while the second appears in UV and in the visible range between 400 and 450 nm. This second contribution interferes with the OH fluorescence signal but arises from a region located outside the methane stream in an intermediate temperature, fuel rich region. It appears that UV laser excitation in high-pressure methane flames may induce simultaneous fluorescence of OH and PAH. In many cases this will not allow a suitable imaging of OH because it will not be possible to discriminate between regions of hydrocarbon pyrolysis and regions of high-temperature oxidation. Because PAH fluorescence covers a broad range of wavelengths, its level may be diminished by adopting a narrowband filtering scheme centered on the OH fluorescence band. As shown in this article, this works well up to a pressure of 2.5 MPa where OH and PAH fluorescence signals feature nearly equal levels as illustrated in Fig. 16. The data points represent the maximum signal levels in representative regions of the image where OH and PAH fluorescence are well separated. As pressure is increased, it is found that PAH and OH fluorescence levels evolve in opposite directions. The photophysics of the PAH fluorescence are less well established than those of OH but it is likely that the fluorescence process involves a single photon absorption step followed by fluorescence. The quantum yield of the process is dominated by quenching as is the case of OH. It is then most probable that the corresponding signal is enhanced with pressure because the PAH mole fraction increases. This is confirmed by experiments [21] on premixed sooting ethylene-air flames in which the total PAH volume fraction increases linearly with pressure at least in the range covered in this investigation (2 MPa). This increase of the PAH mole fraction translates into an increasing UV fluorescence intensity level balanced by the fluorescence quantum yield but this cannot be estimated precisely. There is a general lack of high-temperature absorption data for polycyclic aromatic hydrocarbons and there are no detailed species profile measurements in the high-pressure flames examined in the present experiments.

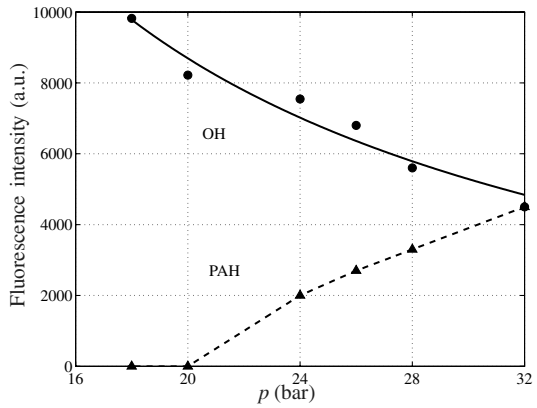


**Fig. 16 Pressure dependence of the OH and hydrocarbon fluorescence signal for $LOx/GCH_4$ cryogenic flames. Circles: OH fluorescence; triangles: PAH fluorescence. The two signals take equal values at a pressure of 3.2 MPa.**

The OH fluorescence intensity decreases by approximately a factor of 2 between 1.7 and 3.2 MPa. This is determined by measuring the signal level in the lower part of the flame which is closest to the window used to transmit the laser sheet into the chamber. Laser attenuation is minimized in this region while the level of OH fluorescence decreases. On the other hand, the amplitude of PAH fluorescence in the UV range increases and one may also assume that a part of the laser fluence is absorbed by intermediate hydrocarbon species. The optical depth diminishes as pressure increases due to 1) an increase in PAH mole fraction, and 2) attenuation in the OH layer. There are also some recent indications [5] that in high-pressure, high-temperature combustion environments, the UV transmission is reduced by absorption by species like $CO_2$ and $H_2O$. This attenuates the incident laser fluence and the resulting fluorescence intensity. The combination of these various processes reduces the optical depth setting limitations to the method. In practice Fig. 16 indicates that there is a crossover point where the useful OH fluorescence signal is dominated by the interference from PAH fluorescence. This sets the upper limit to the OH–PLIF technique to about 2.5 MPa in this case of study.

To obtain useful OH fluorescence data beyond that pressure would require a more elaborate excitation/detection setup. One possibility would be to use two lasers, the first tuned on a resonant transition of OH, the second radiating at a slightly shifted nonresonant wavelength. The laser pulses would be delayed in time by about 50 ns allowing successive detection by two gated ICCD cameras. It would then be possible to subtract the second image (PAH fluorescence) from the first one (OH and PAH fluorescence). The method would not work without a preliminary calibration to suppress effects of laser sheet inhomogeneities. It would be even better to simultaneously measure the pulse energies and spatial distributions of light intensity in the two laser sheets. However the complexity of this scheme and the amount of equipment required might not allow its practical implementation.

## V. Conclusions

Laser-induced fluorescence experiments have been carried out on high-pressure liquid oxygen/methane flames. Using a narrowband detection scheme it has been possible to obtain good quality images at pressures below 2.5 MPa. Beyond that limit an additional fluorescence signal originating from PAH species formed outside the flame zone interferes with the OH fluorescence and scrambles the useful signal.

For $LOx/GH_2$ flames, the absorption of the laser energy is the limiting factor for high-pressure OH–PLIF application. When gaseous methane is coaxially injected around the liquid oxygen jet, the limiting factor is much more the UV PAH fluorescence. At the low mixture ratios used in the present experiments, OH and PAH fluorescence cannot be distinguished above $\simeq$ 2.5 MPa.

In the accessible pressure range (below 2.5 MPa) OH fluorescence images indicate that the flame develops as a thin wrinkled layer spreading near the liquid oxygen jet. The flame edge lies at a distance from the injector lip indicating that the reactive region is sensitive to the flow perturbations and that the flame is less well stabilized than liquid oxygen/hydrogen flames investigated in previous studies.

## Acknowledgments

This work was supported by Centre National d'Etudes Spatiales (CNES), Snecma, Centre National de la Recherche Scientifique (CNRS), and the Institut Universitaire de France. The help of the Mascotte team of ONERA is gratefully acknowledged. Reviewer comments have been greatly appreciated.

## References

[1] Seitzman, J. M., Ungut, A., Paul, P. H., and Hanson, R. K., "Imaging and Characterization of OH Structures in a Turbulent Nonpremixed Flame," *Proceedings of the Combustion Institute*, Vol. 23, No. 1, 1990, pp. 637–644.

[2] Donbar, J. M., Driscoll, J. F., and Carter, C. D., "Reaction Zone Structure in Turbulent Non Premixed Jet Flames—From CH-OH PLIF Images," *Combustion and Flame*, Vol. 122, No. 1–2, 2000, pp. 1–19.

[3] Kohse-Hoinghaus, K., "Laser Techniques for the Quantitative Detection of Reactive Intermediates in Combustion Systems," *Progress in Energy and Combustion Science*, Vol. 20, No. 3, 1994, pp. 203–279.

[4] Battles, B. E., and Hanson, R. K., "Laser-Induced Fluorescence Measurements of NO and OH Mole Fraction in Fuel Lean, High Pressure (1–10 atm) Methane Flames: Fluorescence Modeling and Experimental Validation," *Journal of Quantum Spectroscopy and Radiative Transfer*, Vol. 54, No. 3, 1995, pp. 521–537.

[5] Schultz, C., Jeffries, J., Davidson, D. F., Koch, J. D., Wolfrum, J., and Hanson, R. K., "Impact of UV Absorption by $CO_2$ and $H_2O$ on NO LIF in High Pressure Combustion Applications," *Proceedings of the Combustion Institute*, Vol. 29, No. 2, 2002, pp. 2735–2742.

[6] Singla, G., Scouflaire, P., Rolon, J. C., and Candel, S., "Planar Laser Induced Fluorescence of OH in High Pressure Cryogenic $LOx/GH_2$ Jet Flames," *Combustion and Flame*, Vol. 144, No. 1–2, 2006, pp. 151–169.

[7] Singla, G., Scouflaire, P., Rolon, J. C., and Candel, S., "Transcritical Oxygen/Transcritical or Supercritical Methane Combustion," *Proceedings of the Combustion Institute*, Vol. 30, No. 2, 2005, pp. 2921–2928.

[8] Snyder, R., Herding, G., Rolon, J. C., and Candel, S., "Analysis of Flame Patterns in Cryogenic Propellant Combustion," *Combustion Science and Technology*, Vol. 124, No. 1–6, 1997, pp. 331–370.

[9] Luque, J., and Crosley, D. R., "LIFBASE: Database and Spectral Simulation Program," Tech. Rept., Ver. 2.02, SRI International Rept. MP 99-009, 1999.

[10] Herding, G., Snyder, R., Rolon, C., and Candel, S., "Investigation of Cryogenic Propellant Flames Using Computerized Tomography of Emission Images," *Journal of Propulsion and Power*, Vol. 14, No. 2, 1998, pp. 146–151.

[11] Rehab, H., Villermaux, E., and Hopfinger, E., "Flow Regimes of Large Velocity Ratio Coaxials Jets," *Journal of Fluid Mechanics*, Vol. 345, Aug. 1997, pp. 357–381.

[12] Ni, T., Pinson, J. A., Gupta, S., and Santoro, R. J., "Two Dimensional Imaging of Soot Volume Fraction by the Use of LII," *Applied Optics*, Vol. 34, No. 3, 1995, pp. 7083–7091.

[13] Shaddix, C. R., and Smyth, K. C., "Laser Induced Incandescence Measurements of Soot Production in Steady and Flickering Methane, Propane, and Ethylene Diffusion Flames," *Combustion and Flame*, Vol. 107, No. 4, 1996, pp. 418–452.

[14] Meyer, T. R., Roy, S., and Belovich, V. M., Corporan, E., and Gord, J. R., "Simultaneous Planar Laser-Induced Incandescence, OH Planar Laser-Induced Fluorescence, and Droplet Mie Scattering in Swirl-Stabilized Spray Flames," *Applied Optics*, Vol. 44, No. 3, 2005, pp. 445–454.

[15] Beretta, F., Cincotti, V., D'Alessio, A., and Menna, P., "UV and Visible Fluorescence in the Fuel Pyrolysis Regions of Gaseous Diffusion Flames," *Combustion and Flame*, Vol. 61, No. 3, 1985, pp. 211–218.

[16] Allen, M. G., McManus, K. R., Sonnenfroh, D. M., and Paul, P. H., "Planar Laser-Induced-Fluorescence Imaging Measurements of OH and Hydrocarbon Fuel Fragments in High Pressure Spray-Flame Combustion," *Applied Physics B: Lasers and Optics*, Vol. 34, No. 27, 1995, pp. 6287–6300.

[17] Smyth, K. C., Shaddix, C. R., and Everest, D. A., "Aspects of Soot Dynamics as Revealed by Measurements of Broadband Fluorescence and Flame Luminosity in Flickering Diffusion Flame," *Combustion and Flame*, Vol. 111, No. 3, 1997, pp. 185–207.

[18] Böhm, H., Kohse-Höinghaus, K., Lacas, F., Rolon, C., Darabiha, N., and Candel, S., "On PAH Formation in Strained Counterflow Diffusion flames," *Combustion and Flame*, Vol. 124, No. 1–2, 2001, pp. 127–136.

[19] Raiche, G. A., and Jeffries, J. B., "Laser-Induced Fluorescence Detection of Polycyclic Aromatic Hydrocarbons in dc Arcjet Used for Diamond Deposition," *Applied Physics Letters*, Vol. 63, No. 22, 1993, pp. 3002–3004.

[20] Ciajolo, A., Tregrossi, A., Barbella, R., Ragucci, R., Apicella, B., and De Joannon, M., "The Relation Between Ultraviole-Excited Fluorescence and Aromatic Species Formed in Rich Laminar Ethylene Flames," *Combustion and Flame*, Vol. 125, No. 4, 2001, pp. 1225–1229.

[21] Bonig, M., Felderman, C., Jander, H., Luers, B., Rudolph, G., and Wagner, H., "Soot Formation in Premixed $C_2H_4$ Flat Flames at Elevated Pressure," *Proceedings of the Combustion Institute*, Vol. 23, No. 1, 1990, pp. 1581–1587.

J. Oefelein
*Associate Editor*